

Distribution Agreement

In presenting this thesis as a partial fulfillment of the requirements for a degree from Emory University, I hereby grant to Emory University and its agents the non-exclusive license to archive, make accessible, and display my thesis in whole or in part in all forms of media, now or hereafter now, including display on the World Wide Web. I understand that I may select some access restrictions as part of the online submission of this thesis. I retain all ownership rights to the copyright of the thesis. I also retain the right to use in future works (such as articles or books) all or part of this thesis.

Josh Peacock

March 25, 2023

Orbital Liquid State in Ultrathin Pt/CoFeB Films

by

Josh Peacock

Sergei Urazhdin
Adviser

Physics

Sergei Urazhdin
Adviser

Hayk Harutyunyan
Committee Member

Jed Brody
Committee Member

Maja Taskovic
Committee Member

2023

Orbital Liquid State in Ultrathin Pt/CoFeB Films

By

Josh Peacock

Sergei Urazhdin

Adviser

An abstract of
a thesis submitted to the Faculty of Emory College of Arts and Sciences
of Emory University in partial fulfillment
of the requirements of the degree of
Bachelor of Science with Honors

Physics

2023

Abstract

Orbital Liquid State in Ultrathin Pt/CoFeB Films

By Josh Peacock

In this work, anomalous results observed in Anomalous Hall Effect and Brillouin Light Spectroscopy measurements of Co/Ni and CoFeB ultrathin films indicate the importance of orbital magnetism in describing these systems. These measurements are considered in the absence of an anomalous feature presence in Magneto-Optic Kerr Effect measurements of the same samples. The theoretical component of this work derives the presence of orbital correlations in ultrathin films of late transition metals, and effects of geometric frustration on a triangular lattice determine that the mismatch between orbital and crystal symmetries results in an orbital liquid state. Comparing solutions from independent-particle techniques, virtual hopping approximation techniques, and numerical simulations, it is evident that the independent-particle model is insufficient to describe our systems and that the virtual hopping approximation is more realistic. Applications of this orbital liquid state to technologically relevant phenomena are discussed, and the role of Pt in our experimental structures is explored.

Orbital Liquid State in Ultrathin Pt/CoFeB Films

By

Josh Peacock

Sergei Urazhdin

Adviser

A thesis submitted to the Faculty of Emory College of Arts and Sciences
of Emory University in partial fulfillment
of the requirements of the degree of
Bachelor of Science with Honors

Physics

2023

Acknowledgements

I thank my adviser, Sergei Urazhdin, for his guidance and contributions throughout this project. I also thank Sergei Ivanov for his CoFeB AHE and MOKE measurements, as well as his collaboration on the numerics required for the theoretical component of this work. We thank V. Demidov and S. Demokritov (University of Münster) for the BLS measurements.

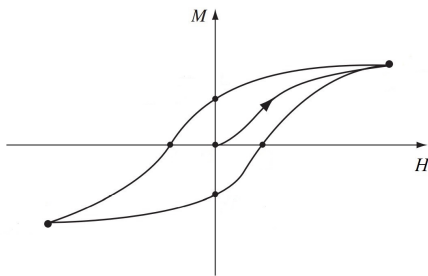
Table of Contents

1 Introduction.....	1
1.1 Motivation	1
1.2 Background	2
1.2.1 Phase transitions and Landau Theory	2
1.2.2 Anomalous Hall effect	3
1.2.3 Magneto-optical Kerr effect	3
1.2.4 Field theoretical language	4
1.2.5 BCS, Mott, and Kugel-Khomskii systems	6
2 Experimental Work	7
2.1 Methods (AHE)	7
2.2 Results and Discussion	8
2.2.1 AHE in Co/Ni films	8
2.2.2 Experimental work of collaborators: AHE in CoFeB films	10
2.2.3 Experimental work of collaborators: MOKE	11
2.2.4 Experimental work of collaborators: BLS	12
3 Theoretical Work	15
3.1 Motivation	15
3.2 Methods	16
3.3 Results and Discussion	17
3.3.1 Orbital correlations	17
3.3.2 Geometric frustration	18
3.3.3 Application to PMA	21
3.3.4 Role of Pt	23
4 Conclusions	24

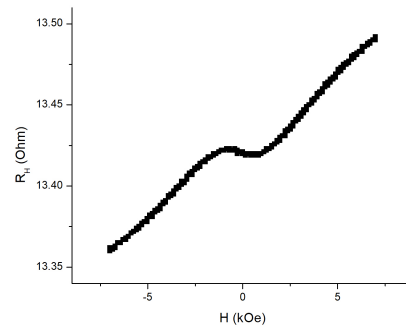
1 Introduction

1.1 Motivation

Inspiration for this work began from the adviser’s observation of an unusual feature in magnetic hysteresis curves of certain multilayer ultrathin films. In other words, a standard magnetic hysteresis loop exhibits linear susceptibility when the applied field is small, as shown in Figure 1a. However, as shown in Figure 1b, some measurements of hysteresis curves for ultrathin films of late transition metals (see Section 2.2) appear to have an unusual “wiggle” added to the typical response.



(a) An example of a (fairly-generic) standard hysteresis loop, adapted from Figure 6.28 of [8]. The x-axis is applied magnetic field, and the y-axis is magnetization.



(b) An observation of the “wiggle” imposed on the standard hysteresis curve. Notice that we expect saturation of the magnetization at large fields, although saturation may be slightly difficult to visualize given the limitations of the maximum field applied.

Figure 1: Comparison between a generic textbook-example magnetization curve and the type of observations that sparked this investigation.

When we started this project, we had only the observation of this strange “wiggle” feature, but no knowledge of its meaning. So, we began investigating the properties and origin of the “wiggle” with experiments, as detailed in Section 2. As the project progressed, other group members and external collaborators became involved, and the results of experimental work were exciting enough to embark on a theoretical project, as detailed in Section 3.

From the fact that magnetism is well understood to be an electron correlation phenomenon, this project hopes to explore the nature of electron correlations in common transition metal ferromagnets. We explore the effects of these correlations on the electronic and magnetic properties of our systems, and investigate the possibility of tuning magnetic properties by varying correlations.

Next, background information is provided for key experimental techniques and theoretical progress.

1.2 Background

1.2.1 Phase transitions

As this work explores experimental and theoretical perspectives on magnetism, many states of magnetism and transitions between them are discussed. Here, we hope to provide relevant definitions to the reader and references to some theory that guided our work.

Consider a classical magnetization vector M which represents the sum of many small magnetic moments inside a material. Now, say we apply an external magnetic field with strength H in a particular direction, and we sweep this strength from its maximum in one direction to its maximum in the other. The response of M as a function of H will vary depending on the magnetic state of the material. For example, in Figure 1a, we see that dM/dH is finite for all H ; that is, there is a nice "smooth" response to a change in H . This is an example of a paramagnetic response.

Note in Figure 1a that at a large enough magnitude of H , the magnetization does not increase in magnitude past a certain point. This is called saturation of the magnetization, and classically we can think about the alignment of all the magnetic moments in the direction of the magnetization, such that there is no possible way to increase the magnetization any more. We can define magnetic susceptibility $\chi = dM/dH$ to simplify the notation, and in the paramagnetic state we expect to observe linear susceptibility χ for reasonably small H before saturation. However, a key observation of Section 1.1 is the breaking of linear susceptibility by the "wiggle," as shown in Figure 1b.

In the context of our M as a function of H measurements, ferromagnetism is observed when dM/dH becomes very large at certain H , and abrupt flipping of the magnetization direction occurs. There is no linear susceptibility for the ferromagnetic state when M is measured against H , as dM/dH is either very large or essentially zero (see 15 K, 40 K, and 80 K measurements of Figure 6a as an example).

For the ultrathin films we study experimentally, a critical temperature determines the boundary between the ferromagnetic and paramagnetic phase. This temperature is known as the Curie temperature (denoted T_C in the discussions of Section 2), and we define some parameters of Section 2 relative to the Curie temperature.

It will be useful to think about the susceptibility relative to the Curie temperature via the Curie-Weiss law [14]. The Curie-Weiss law describes the susceptibility χ as

$$\chi = \frac{C}{T - T_C}, \quad (1)$$

where C is the Curie constant, T is the temperature, and T_C is the Curie or critical temperature. In other

words, $\chi^{-1} \propto (T - T_C)$ according to the Curie-Weiss law. We will think about this relationship in the context of AHE fitting in Section 2.

1.2.2 Anomalous hall effect

As alluded to previously, a large component of the experimental work of this project relies on measuring the magnetization response to applied field. A key technique for this was anomalous hall effect (AHE) magnetoelectronic measurements, and the fundamentals of this technique are discussed below.

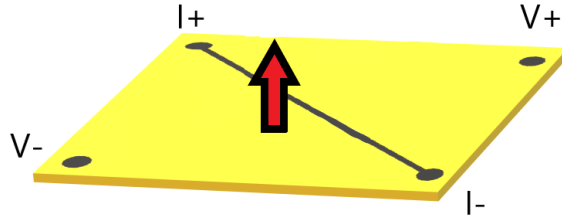


Figure 2: Cartoon representation of the AHE experiment. The yellow plate represents the thin films of this experiment; the red arrow indicates the direction of the applied magnetic field and resulting magnetization of the sample (in this case, out-of-plane). The points labeled $I+$ and $I-$ with the straight line between them show where quasi-DC current is applied and flows, and the points labeled $V+$ and $V-$ are where we observe a voltage difference caused by the AHE.

The AHE can be interpreted as a consequence of the Lorentz force acting on the conduction electrons passing through a magnetic material. The conduction electrons will interact with the applied magnetic field (in Figure 2, the undeflected path of the conduction electrons is the straight line and the applied field and resulting magnetization are in the direction of the red arrows). Some of the conduction electrons will have spin parallel to the direction of the magnetization; some of the electrons will have spin antiparallel to it. In general, the density of conduction electrons for these two cases is not equal, which results in a Hall voltage.

For the purposes of the experiments in Section 2, we are interested in the magnetization of the material. Because the Hall voltage is proportional to the component of magnetization normal to the sample, measuring the Hall voltage gives us a proxy for the magnetization of the sample. Thus, an electronic measurement of the sample can determine the magnetization as a function of applied magnetic field.

1.2.3 Magneto-optical Kerr Effect

Magneto-optical Kerr Effect (MOKE) measurements were performed by a graduate student collaborator [10], and the results of his work are discussed in Section 2. This section, however, provides relevant background to compare and contrast AHE and MOKE, in order to facilitate the simultaneous discussion of these

measurements' results.

There are three types of MOKE experiments – longitudinal, transverse, and polar MOKE. The graduate student collaborator's measurements referenced in this work are polar MOKE measurements. In his experimental setup, linearly polarized light from a Helium-Neon laser source, with wavelength 632.8 nm, is incident normal to the plane of the ultrathin film sample being measured. This film is inside an electromagnet which applies out-of-plane magnetic field relative to the sample, and the resulting magnetization of the sample is out-of-plane also. The light that is reflected back from the sample is redirected towards a camera which measures the relative intensity of the reflected light. This intensity is proportional to the Kerr Angle, which is a proxy for the magnetization of the sample.

Thus, an optical measurement (in the THz frequency range) gives us similar magnetization information as (quasi-DC) AHE measurements. A key difference between MOKE and AHE measurements in this work is that MOKE is insensitive to orbital magnetization, even though MOKE and AHE result from the same chiral current response to electric field [17].

Another optical technique, Brillouin Light Spectroscopy (BLS), was performed by collaborators [10] from the University of Münster. The results of their work is discussed in Section 2, however, specific experimental BLS background information is omitted due to the author's lack of knowledge of the collaborators' experimental apparatus.

1.2.4 Field theoretical language

In this section, important language and conventions for the theoretical component of this work are discussed. Thus, we mainly focus on operators, notation, and applications to simple model systems. The idea is that after these simpler systems are discussed in detail, the more complicated systems of Section 3 will become intuitive.

For the systems discussed in this work, the most efficient way to describe the behavior of many-particle systems is through operators which describe the transition between quantum states in the Fock space. For example, consider the creation operator c^\dagger and the annihilation operator c , which will be used frequently in Section 3. For the systems of this work, the operators will act on fermions, i.e., particles which obey the Pauli exclusion principle and fermionic statistics. Because of electron-hole symmetry, we can choose to describe either electrons or holes with operator language. Since the states of Section 3 are almost filled with electrons, we use the hole representation for simplicity.

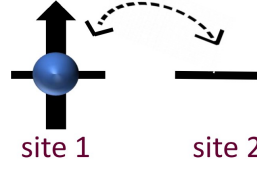


Figure 3: A simple system, analyzed as a worked example in Section 1.2.4.

A simple example [16] may help demonstrate applications of this formalism. Consider a system where one particle (for example, a hole) can hop between two sites; Figure 3 shows a diagram of this system (which is essentially the simplest usage of the tight-binding model). Ultimately, we want to describe the energies of quantum states, so we apply the eigenvalue problem

$$\hat{H}\psi = E\psi, \quad (2)$$

where \hat{H} is the Hamiltonian operator, ψ is a state, and E is the energy of the state. Then using the operator formalism, if t is the kinetic energy of a particle hopping between sites and the subscripts of the operators represent the states on which they are applied, then

$$\hat{H} = t(c_1^\dagger c_2 + c_2^\dagger c_1). \quad (3)$$

In Dirac notation, the basis states are

$$\begin{cases} \psi_1 = c_1^\dagger |0\rangle \\ \psi_2 = c_2^\dagger |0\rangle \end{cases}. \quad (4)$$

From this we construct the system

$$\begin{cases} \hat{H}\psi_1 = t\psi_2 \\ \hat{H}\psi_2 = t\psi_1 \end{cases}, \quad (5)$$

or in matrix form, we act on the basis states with the operator

$$\hat{H} = \begin{pmatrix} 0 & t \\ t & 0 \end{pmatrix}. \quad (6)$$

The eigenstates are

$$\psi_{1,2} = \frac{1}{\sqrt{2}}(c_1^\dagger \pm c_2^\dagger) |0\rangle \quad (7)$$

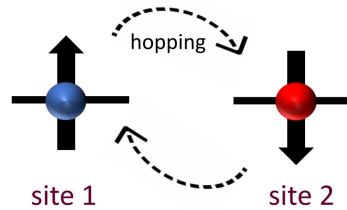
with energy $E = \pm t$. This example demonstrates that the operator formalism allows determination of

the energies accessible to our quantum system, and in this particular example, the energies correspond to bonding/anti-bonding that breaks the degeneracy of atomic orbital energies. In Section 3, we analytically and numerically solve larger matrices and more intricate systems.

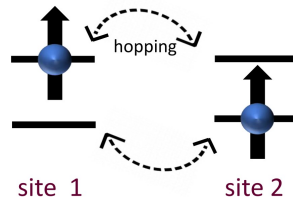
1.2.5 BCS, Mott, and Kugel-Khomskii systems

This section provides some brief history and background about many-particle phenomena in condensed matter physics that have been studied long before this work. For example, in the field of superconductivity over four decades passed between the experimental discovery of superconductivity [12] by H.K. Onnes in 1911 and the first successful theory of superconductivity [1] by Bardeen, Cooper, and Schieffer (BCS) in 1957. Importantly, between 1911 and 1957, many people made unsuccessful attempts to explain superconductivity as a single-particle effect. Only with the Cooper pair, a two-particle correlation introduced with BCS theory, could any progress be made on the subject.

Other well-studied models of correlations in magnetism have been formulated, and these models, namely Mott correlations [4] and Kugel-Khomskii correlations [13], were a starting point and inspiration for much of the theoretical work of Section 3. In Mott correlations, consider a one-orbital system with an average population of one particle per site, as shown in Figure 4a. The Pauli exclusion principle allows hopping between two sites if the spins of the particles on those sites are antiparallel. The result of this is antiferromagnetic (AFM) ordering.



(a) Cartoon schematic of Mott correlations.



(b) Cartoon schematic of Kugel-Khomskii correlations.

Figure 4: Diagrams of Mott and Kugel-Khomskii correlated systems. For each system, only two sites (out of the many sites in a real material) are shown. For visualization purposes, blue indicates a spin-up particle, and red a spin-down particle.

Kugel-Khomskii correlations [13] consider ferromagnetic insulators with two orbitals and an average population of one particle per site, as shown in Figure 4b. Suppose the particles predominantly hop within the same orbital. Then the on-site energy is minimized by Hund's rules if the particles have parallel spins but are on opposite orbitals.

These systems are relevant to our work because they emphasize the importance of considering electron

correlations in our models. We can take what we learned from these models and apply it to analysis of ultrathin films of late transition metals, as detailed in Section 3.

2 Experimental work

2.1 Methods (AHE)

In the onset of this project, the author and adviser conducted anomalous hall effect (AHE) experiments on ultrathin films of late transition metals, starting with Co/Ni as the primary material of study (later, a graduate student collaborator performed similar measurements on CoFeB, see Section 2.2.2. The multi-layer structures in his experiments are slightly different than the ones in this explanation, but the general measurement technique is the same). These ultrathin films were produced using DC and RF sputtering, and the thickness of each deposited layer could be reasonably controlled. Figure 5 shows an example of an Co/Ni-style sample prepared for AHE measurements.

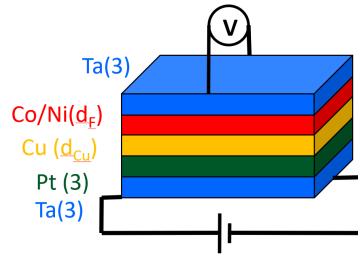


Figure 5: A typical sample used in our preliminary AHE measurement experiments for Co/Ni thin films, including the original Cu spacing layer. The layer names are labeled on the left, and placement of the current applied and voltage measured are diagrammed at the bottom and top, respectively. Note that the thicknesses in parentheses are in units of nm, and typically d_F and d_{Cu} were between 0.3 and 2 nm. This figure was created by the adviser [18].

For the measurements of AHE in Co/Ni, we explored and applied AHE measurements to many compositions of these ultrathin films, mainly by varying the thickness of the Co/Ni layer (d_F) and the thickness of the Cu layer (d_{Cu}). For each sample, AHE scans were performed over a range of temperatures between 12 K and 320 K. By scanning over a range of temperatures for many ultrathin film compositions, we were able to investigate both the composition dependence and temperature dependence of the "wiggle" feature.

2.2 Results and Discussion

2.2.1 AHE in Co/Ni films

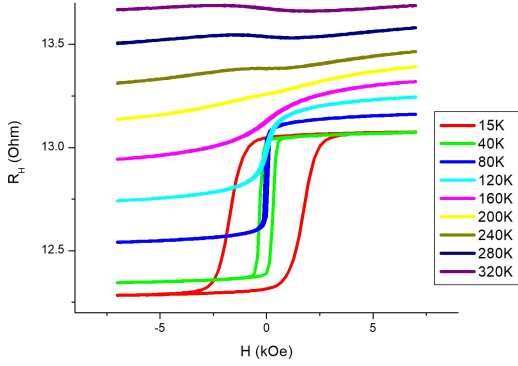
Figure 6a shows an example of a clean AHE scan, where the scan is performed over a range of temperatures from 15 K to 320 K. From these measurements, we are interested in the response of the "wiggle" to changes in temperature and composition. Thus, we define the fitting function

$$R_H = A_1 \arctan\left(\frac{H}{\chi_1^{-1}}\right) + A_2 \arctan\left(\frac{H}{\chi_2^{-1}}\right) + R_0, \text{ where } \chi_1^{-1}, \chi_2^{-1} \propto (T - T_C) \quad (8)$$

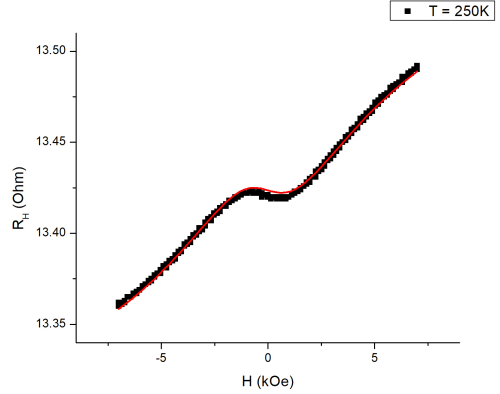
as the fitting function when the "wiggle" is present, and

$$R_H = A_1 \arctan\left(\frac{H}{\chi_1^{-1}}\right) + R_0, \text{ where } \chi_1^{-1} \propto (T - T_C) \quad (9)$$

as the fitting function when the "wiggle" is not present, where R_H is the Hall resistance measured, A_1 and A_2 are fitting "amplitudes", χ_1^{-1} and χ_2^{-1} are proportional to $T - T_C$, and R_0 is a signal offset that was ignored. When the "wiggle" is present, we chose a sum of two arctangents, Equation (8), as the fitting function for two main reasons. The first reason is that enforcing opposite signs between A_1 and A_2 allows for the "wiggle" to be modeled by one amplitude and width, and the "overall" response to be modeled by the other amplitude and width. The other is that we expect saturation of the magnetization at large fields. When the "wiggle" is not present, its features cannot be captured, so we fit with Equation (9).



(a) Raw results of the AHE measurements on the Co/Ni sample over a range of temperatures. For visualization purposes, only 1/4 of the total measurements of this sample are shown. The offset of R_H is arbitrary and essentially ignored, as we are interested in extracting the relative signal features for each temperature. In this form, one can see the transition from ferromagnetic to paramagnetic to paramagnetic+”wiggle” as temperature increases.



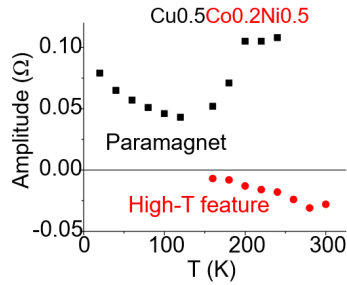
(b) Fitting Equation (8) to this sample’s AHE measurement at a temperature of 250 K. This fit captures the ”wiggle” nicely, and the relevant fitting parameters are $A_1 = 0.15 \pm 0.01$, $\chi_1^{-1} = 5600 \pm 800$, $A_2 = (-0.05) \pm 0.01$, $\chi_2^{-1} = 1700 \pm 300$, where A_1 and A_2 are in units of Ohms and the units of χ_1^{-1} and χ_2^{-1} are arbitrary.

Figure 6: Results and fitting of an AHE measurement of a sample with composition Ta(2)Pt(2)Cu(1.5)Co(0.4)Ni(0.4)Ta(2), where the thicknesses in parentheses are in nm.

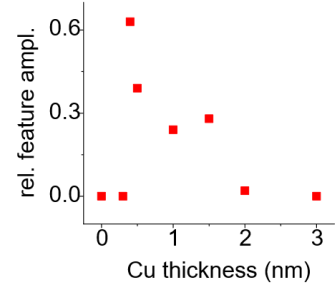
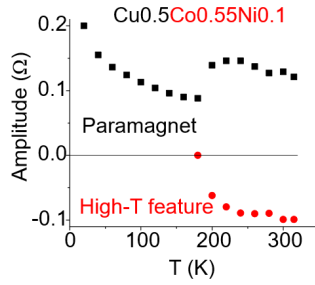
For many samples, we fit Equation (8) and Equation (9) to the measurement at each temperature (for example, all the measurements shown in Figure 6a plus the measurements omitted from the figure for visual purposes).

We consider many other sample compositions of interest, namely by varying d_F and d_{Cu} as defined in Figure 5. Figure 7a shows an example of adjusting the relative thickness of Co and Ni while keeping the thickness of the Cu spacer the same. Conversely, Figure 7b shows the ”wiggle” amplitude as a function of d_{Cu} , keeping d_F constant at 0.35 nm Co, 0.35 nm Ni. We see that below a d_{Cu} of 0.3 nm, there is no ”wiggle” at all. When d_{Cu} is just greater than this threshold, we achieve the maximum ”wiggle” amplitude, and as d_{Cu} increases, the ”wiggle” amplitude decays to 0 by about $d_{Cu} = 3$ nm.

These observations suggest that there is an extreme sensitivity of the ”wiggle” feature to d_F , d_{Cu} and the multilayer composition. The collective properties of the ultrathin layers contribute to this feature; this observation points to electron correlation effects. At the onset of this project, the author and adviser did not know anything about the nature of the observed feature; the experimental results guided us towards the correlated electron physics that best describe ultrathin films of late transition metals. However, much of the remainder of this experimental work considers CoFeB-based films instead of Co/Ni-based films.



(a) An example of varying the relative thickness of Co and Ni. Thicknesses are shown above the caption, in units of nm. It is clear that the behavior of the "wiggle" is sensitive to the Co/Ni layer's properties and composition.



(b) The impact of the width of the Cu layer on the "wiggle" amplitude. There is a critical transition at 0.3 nm, below which the "wiggle" feature is not present.

Figure 7: An example of the sensitivity of the "wiggle"'s properties to the composition. Notice the extreme impacts of varying the Co/Ni ratio or thickness of the Cu layer.

2.2.2 Experimental work of collaborators: AHE in CoFeB films

A graduate student collaborator [10] took similar AHE measurements on films with a CoFeB instead of the Co/Ni layer discussed in the previous section. The results, shown in Figure 8, are generally in agreement with the observations for thin films of Co/Ni.

From Figure 8b, we can clearly see the efficacy of the two order parameter Landau fitting, as in Equation (8) and Equation (9), at describing the "wiggle" feature. Figure 8c shows another concrete example of the $T - T_C$ order parameter and its extrapolation. For example, the first critical temperature $T_{C1} = 131\text{K}$, reasonably corresponds to the Curie temperature of the sample. This makes sense, since as was discussed in Section 1, crossing the Curie temperature is an example of a magnetic phase transition. $T_{C2} = 168\text{K}$ extrapolates to a much higher temperature, and we can think about this as the onset of the "wiggle" feature (which we only observe at high temperatures).

The key conclusions from both the Co/Ni and CoFeB AHE experiments are the presence of the "wiggle" feature at high temperatures and the extraction of two order parameters with different transition temperatures. These magnetic order parameters are shown to be independent and will be explored in the context of other collaborator's supporting experiments.

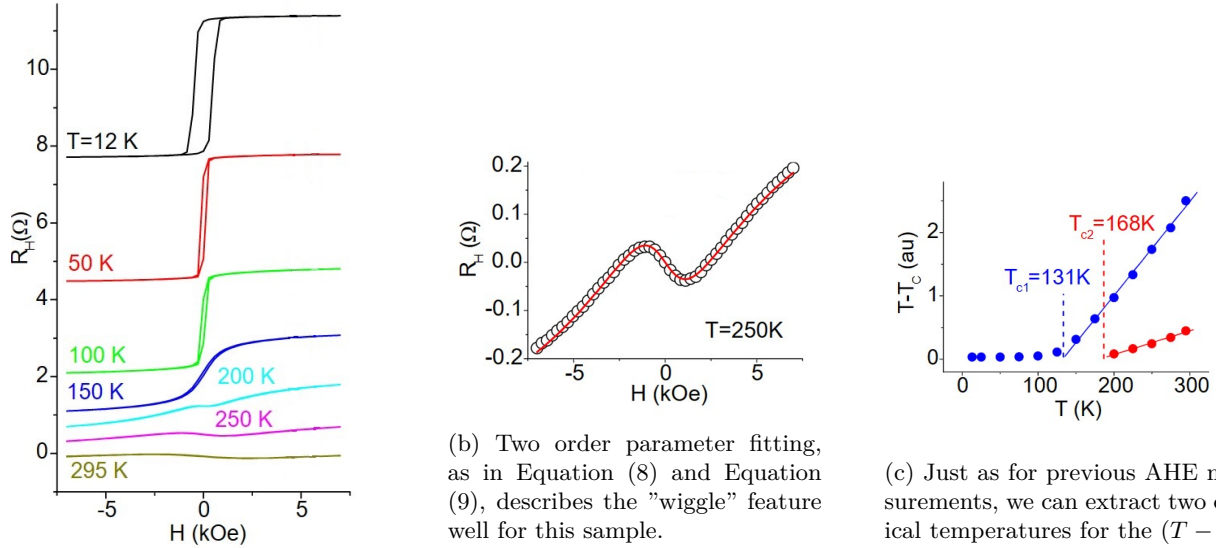
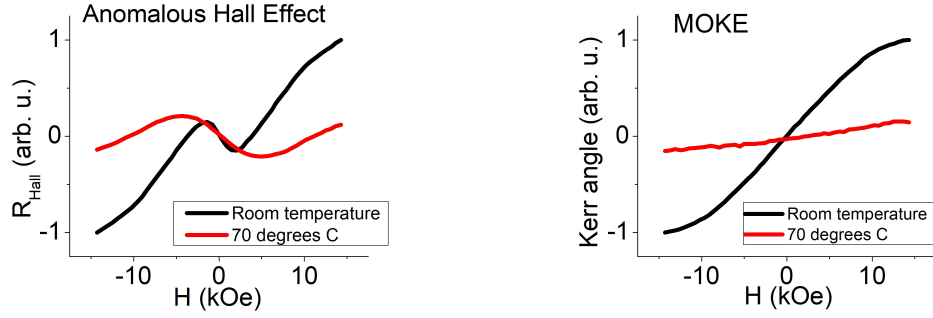


Figure 8: AHE measurements and fittings for a sample with composition $\text{Ti}(1.5)\text{Pt}(1.5)\text{CoFeB}(0.6)\text{Ta}(3)$.

2.2.3 Experimental work of collaborators: MOKE

Around the same time as the previously-discussed AHE measurements were performed, a graduate student collaborator [10] performed simultaneous AHE and Magneto-optical Kerr Effect (MOKE) measurements on an ultrathin film with composition $\text{Ti}(1.5)\text{Pt}(2)\text{CoFeB}(0.35)\text{AlOx}(3)$, where thicknesses are in nm. The most important components of this structure are the layer of Pt and the layer of CoFeB. Results of the AHE and MOKE measurements are shown in Figure 9.

Although the measurement techniques of AHE and MOKE are very similar, we observe qualitatively different results for the two techniques when applied to this sample. In the AHE measurement, the "wiggle" feature is present at both room temperature and 70°C , but we see no evidence of the "wiggle" in the MOKE measurements.



(a) AHE measurement of this structure, where the measurements are dominated by paramagnetic behavior at 293 K and by the "wiggle" at 70°C.

(b) MOKE measurements for this structure, which show only a paramagnetic response with no evidence for anomalous behavior.

Figure 9: A graduate student collaborator's [10] MOKE measurements of a film structure with composition $\text{Ti}(1.5)\text{Pt}(2)\text{CoFeB}(0.35)\text{AlOx}(3)$, where thicknesses are in nm.

The qualitative difference in results across AHE and MOKE is somewhat surprising, since both result from the same chiral current response to electric field. Yet the absence of the feature in the MOKE measurements suggests that the two order parameters in these systems originate from different materials and mechanisms.

2.2.4 Experimental work of collaborators: BLS

Our group is fortunate to have collaborated with researchers at the University of Münster [10] who provided us with Brillouin Light Spectroscopy (BLS) measurements of similar CoFeB-based ultrathin multilayer structures. Figure 10 shows an optical micrograph of the sample used for BLS measurements.

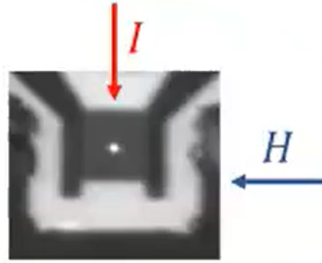


Figure 10: An optical micrograph of a sample used for BLS measurements. Current I and in-plane magnetic field H are applied as shown. The width of the image is several μm .

Figure 11 shows the results and post-processing of the BLS measurements. The fittings in Figure 11c and Figure 11d were performed using the Kittel formula,

$$f = \frac{g\mu_B}{2\pi\hbar} \sqrt{H(H + M_{eff})}, \quad (10)$$

where f is the frequency, g is the Landé g-factor, H is the applied magnetic field, and M_{eff} is the net anisotropy. In this work, a working definition of the Landé g-factor as

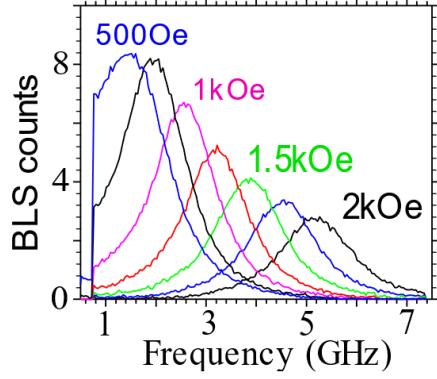
$$g = \frac{J(J+1) + S(S+1) - L(L+1)}{2J(J+1)}, \quad (11)$$

ie, dependent on the spin angular momentum S , orbital angular momentum L , and total angular momentum J , is used.

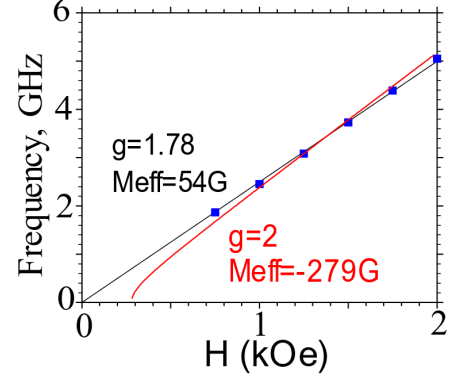
The results of our collaborators' BLS measurements are quite striking. Firstly, the g-factor of 1.78 at 0 current, as shown in Figure 11d, is anomalously low compared to the theoretical value of $g \approx 2$. Near the end of Section 3, possible theories for this low g-factor are explored.

Moreover, fittings of Equation (10) show a strong dependence of both the Landé g-factor and net anisotropy on current. Variations in these quantities show variations in the relative orientation and magnitude of the spin and orbital moments, as shown in Figures 11c and 11d. For example, a low g-factor (less than 2) indicates that the spin and orbital moments are aligned and of similar magnitude, whereas a higher g-factor (greater than 2) indicates anti-alignment of the spin and orbital moments.

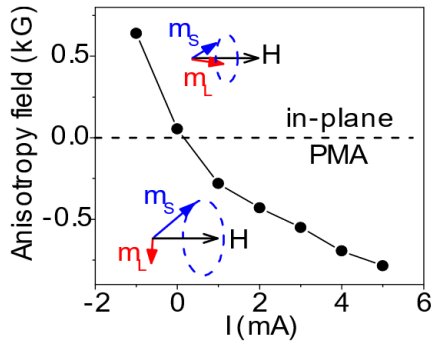
These BLS measurements point to signatures of orbital magnetism in our ultrathin thin films of late transition metals. Contributions of orbital magnetism, elucidated by BLS measurements, are consistent with the signature of the "wobble" in AHE measurements of CoFeB and the lack of a "wobble" signature in MOKE measurements of the same sample. Thus, the theoretical work of this project begins with conceptions of orbital magnetism observed experimentally and develops a model for an orbital liquid state that would agree with the measurements discussed in Section 2.



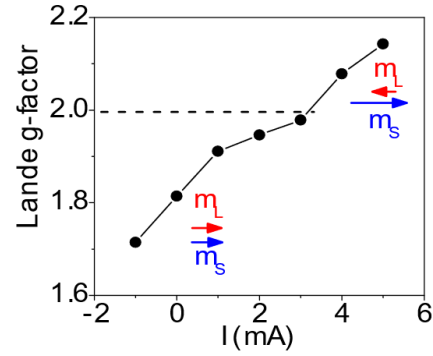
(a) Raw BLS measurements of thermal fluctuation spectra at zero current. The measurements are well-described by Lorentzian peaks.



(b) Dependence of peak BLS frequency on applied magnetic field. The black and red curves represent fitting by Equation (10).



(c) Dependence of the anisotropy on current, as a result of fitting using Equation (10). The inset diagrams indicate the relative orientation of the applied field H , spin moment m_s , and orbital moment m_L , in each regime.



(d) Dependence of the Landé g -factor on current, as a result of fitting using Equation (10). The arrow diagrams indicate the orientation and relative magnitude of the spin and orbital moments.

Figure 11: BLS measurements and fitting performed by collaborators at the University of Münster [10]. The results of these measurements have been presented in [10, 17].

3 Theoretical work

3.1 Motivation

By this point in the project, it was clear that we had novel experimental results, but we started out with limited theoretical understanding of the effects observed. The experimental evidence of Section 2 largely points to the role of orbital effects resulting in magnetism, and guided us towards investigating orbital correlations that we expected to play a role in our systems. The results are even more exciting than we expected when we undertook the theoretical studies that follow.

The following discussion largely parallels the theoretical work published earlier this year by our group [11], which blossomed into its own separate paper even though it was originally intended to supplement an experimental paper. In this work, we hope to clarify mechanisms of ferromagnetism in ultrathin films of late transition metals and to make fundamental and technologically relevant predictions.

The theoretical work of this project [11] sought to explore orbital correlations in ultrathin films of late transition metals which were discussed experimentally in Section 2. As foreshadowing, below is a key result, the mechanism of ferromagnetism identified in our system as shown in Figure 12.

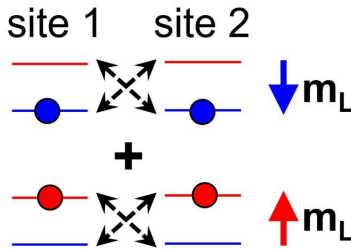


Figure 12: A central result of the theoretical analysis of this work, showing ferromagnetic singlet orbital correlations in late transition metal films. Two sites are used for visualization purposes. Figure is from [17].

Compare Figure 12 to the Mott and Kugel-Khomskii systems in Figure 4. In our mechanism, opposite-orbital hopping is dominant. Virtual hopping stabilizes an orbital singlet state, which can be described as an orbital liquid [11]. The subsequent derivation shows how we arrive at this mechanism and the implications of this model. Additionally, the role of Pt (and the Pt/CoFeB interface) is explored and adds another layer of complexity to the analysis.

3.2 Methods

We start with the Hubbard-Kanamori model in the hole representation [11],

$$\begin{aligned}
\hat{H} = & \sum_{\vec{n}, \vec{l}, \sigma, \sigma', s} t_{\vec{n}, \vec{n}+\vec{l}}^{\sigma, \sigma'} \hat{c}_{\vec{n}+\vec{l}, \sigma', s}^\dagger \hat{c}_{\vec{n}, \sigma, s} + U \sum_{\vec{n}, \sigma} \hat{n}_{\vec{n}, \sigma, \uparrow} \hat{n}_{\vec{n}, \sigma, \downarrow} + U' \sum_{\vec{n}, \sigma} \hat{n}_{\vec{n}, \sigma, \uparrow} \hat{n}_{\vec{n}, -\sigma, \downarrow} + \\
& + U'' \sum_{\vec{n}, s} \hat{n}_{\vec{n}, +, s} \hat{n}_{\vec{n}, -, s} + J \sum_{\vec{n}, \sigma} \hat{c}_{\vec{n}, \sigma, \uparrow}^\dagger \hat{c}_{\vec{n}, -\sigma, \downarrow}^\dagger \hat{c}_{\vec{n}, \sigma, \downarrow} \hat{c}_{\vec{n}, -\sigma, \uparrow} + \\
& + J_c \sum_{\vec{n}, \sigma} \hat{c}_{\vec{n}, \sigma, \uparrow}^\dagger \hat{c}_{\vec{n}, \sigma, \downarrow}^\dagger \hat{c}_{\vec{n}, -\sigma, \downarrow} \hat{c}_{\vec{n}, -\sigma, \uparrow} + \sum_{\vec{n}, s, s', \sigma, \sigma'} \lambda_{s, s'}^{\sigma, \sigma'} \hat{c}_{\vec{n}, \sigma, s}^\dagger \hat{c}_{\vec{n}, \sigma', s'}, \quad (12)
\end{aligned}$$

where we have used operator language so \hat{c}^\dagger creates a hole, \hat{c} annihilates a hole, \hat{n} is the number operator, and summation is over the dummy indices as defined. Note that $\sigma = \pm$ enumerates the orbitals d_{+2}, d_{-2} . The first term in Equation (12) is a hopping term, the next two terms are spin-orbit interaction, and all remaining terms are hole-hole interactions. The last term accounts for spin-orbit coupling (SOC), which is ignored for now but discussed later in Section 3.

Symmetry requirements [19] constrain the relationships between the parameters U, U', U'', J , and J_C in Equation (12). These relationships are basis-dependent, and let $U_0 = 3.64$ eV and $J_0 = 0.77$ eV based on prior modeling [3, 15]. In the orbital basis of cubic harmonics, $U = U_0 + J_0/2$, $U' = U_0 - J_0/2$, $U'' = U_0 - J_0$, and $J = J_C = J_0/2$. In the orbital basis of spherical harmonics, $U = U' = U_0$, $U'' = U_0 - J_0$, $J = J_0$, and $J_C = 0$.

Next, we apply Equation (12) to solve simple models that help us gain intuition about the system. These simple models are a two-site and three-site model, each with two orbitals and an average population of one hole per site. There are two main avenues for solving the two-site and three-site models. The first is using analytic methods where a solution is determined by hand, taking advantage of symmetries. The adviser is primarily responsible for the analytic calculations to follow. An alternative to analytic calculations are numerical approximations, largely performed by the author and a graduate student collaborator.

To do numerical calculations (the author preferred Python, the graduate student collaborator preferred C++), we considered every possible state that was available to the two-site or three-site model given an arbitrary number of particles in the system. For example, in the two-site model with two particles, there were 66 available states. We then considered what would happen transitioning from a given state to every other state in the system, applying Equation (12) to each transition. Importantly, we enabled the parameters defined above (U, J , etc. following the relationships required by symmetry) to be passed to functions in the programs, so that we could analyze the response of state energy as a function of interaction U , for example.

We considered a list of many interactions U between 0 eV and 6 eV (the upper limit being well above

the realistic U_0). For each U , we applied the Hamiltonian to the state, and computed the eigenvalues in accordance with Equation (2). The Hamiltonian is Hermitian, so the eigenvalues are real. We considered the minimum eigenvalue from each of these matrices, to numerically evaluate the energy of the ground state as a function of U . Numerical calculations were compared to analytic expressions derived by the adviser, as discussed in the next section.

3.3 Results and Discussion

3.3.1 Orbital correlations

In [11], the adviser showed analytically that the following d-level diagram describes our late transition metal films well in the ultrathin limit. The details are omitted in this work, but for Co, about one d-hole per site is considered. It turns out that there are two dominant orbitals, d_{+2} and d_{-2} . This result (shown in Figure 13) will be of importance later in this discussion, when the crystal field symmetries are contrasted with geometric frustration.

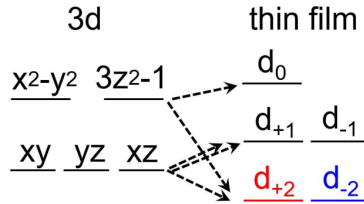


Figure 13: Splitting of d-levels, as a result of symmetries arising from the face-centered-cubic (fcc) structure of late transition metals. Figure is from [17].

Next, we consider a model system of two holes on two orbitals, in a two-site approximation. This system turns out to be essentially equivalent to the Kugel-Khomskii system as calculated by the Koster-Slater integrals [9]. The only difference is a small adjustment in the amplitudes of hopping.

Analytic calculations performed by the adviser [11] show that for this model system at negligible interaction $U \rightarrow 0$, the ground state is a single-particle ground state with two opposite-spin holes. At finite interaction U , this state evolves into a singlet whose approximate energy (calculated through perturbation theory [7] and neglecting the last two terms of Equation (12)) is

$$E_0^{(2)} = U/2 - \sqrt{(U/2)^2 + 4t_{x^2-y^2}^2}, \quad (13)$$

where $t_{x^2-y^2} = 0.39$ eV for Co as a result of the Koster-Slater integrals [9, 20]. In the limit of large interaction

U , the ground state is shown to be a spin triplet, where the energy as a function of U in this limit is

$$E_t = U''/2 - \sqrt{(U''/2)^2 + (t_{x^2-y^2} - t_{xy})^2}, \quad (14)$$

where $t_{xy} = -0.33$ eV for Co, again from the Koster-Slater integrals [20]. Note that for the hopping parameters of Ni, $E_t = 0.2$ eV and the state is dominated by the first term in Equation (14). This means the holes are almost localized, in agreement with the analytic calculations performed by the adviser [11]. These results agree with the author and graduate student collaborator's numerical results, as shown in Figure 14.

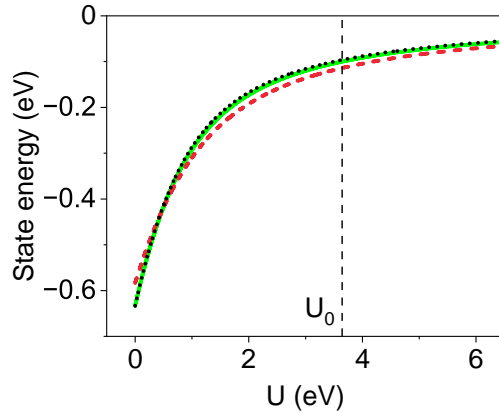


Figure 14: State energy as a function of U in the two-site model (figure is from [11]) with $J_0 = 0.21U_0$, as determined by three techniques using the hopping parameters of Ni. The black dots represent the nonmagnetic singlet described by Equation (13), the red dashes represent the ferromagnetic spin triplet described by Equation (14). The solid green curve is the result of numerical analysis, as described in Section 3.2, for the nonmagnetic state. Fortunately, the numerical computation aligns very closely with the analytic approximation in the low- U and high- U regimes. Note that in the figure, U_0 is the Coulomb interaction energy.

The two-site model was a convenient starting point, however the next logical step in our analysis was to upgrade to three sites on a triangular lattice. A triangular lattice is the most natural two-dimensional model to represent the crystal structure of late transition metals. The next section shows that the similarity to the Kugel-Khomskii model for two sites does not extend to three sites, as a consequence of orbital frustration.

3.3.2 Geometric Frustration

Figure 15 shows the representation of this model in two bases. As can be seen in Figure 15a, the cubic harmonic basis is quite tricky to work with, so used a spherical harmonic basis as shown in Figure 15b. To do this, we transformed site 3 by the Condon-Shortley phase convention. We rotated site 1 by an angle of $2\pi/3$ clockwise, and site 2 by $2\pi/3$ counterclockwise. The advantage of this basis is that the matrix element t_{+-} describes opposite-orbital hopping between any of the sites, which was not the case in the basis of cubic

harmonics. Counterclockwise hopping on the same orbital d_{+2} has an amplitude $e^{-2\pi i/3}t_{++}$, where t_{++} is real, and clockwise hopping on the same orbital has an amplitude $e^{2\pi i/3}t_{++}$. These amplitudes for opposite directions are complex conjugates of each other, which makes sense for a time-reversed process in a Hermitian system. Complex conjugation of the described amplitudes also occurs when considering same-orbital hopping on d_{-2} instead of d_{+2} . We apply the Koster-Slater parameters [20] for holes, and with a precision of about 0.01 eV, we find for Ni, $t_{+-} = 0.29$ eV, $t_{++} = 0.3$ eV, and for Co, $t_{+-} = 0.36$ eV, $t_{++} = 0.3$ eV.

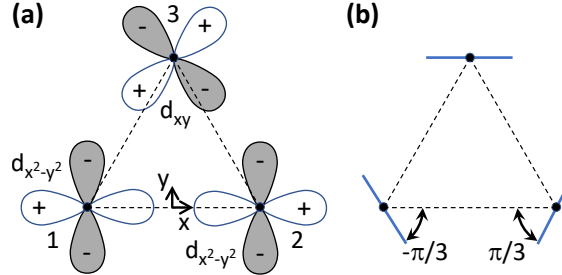


Figure 15: Diagram of the three-site model, figure is from [11]. (a) Visualization of the orbitals on the lattice in the basis of cubic harmonics. (b) Rotated spherical harmonic basis, where the blue lines represent the real and positive axis.

With three particles in the system, the adviser's analytic calculations showed that in the limit of small U , we can approximate

$$E_3 = -4t_{+-} - t_{++} + 2U''/3. \quad (15)$$

He also showed through second-order perturbation theory [7] that in the high- U limit where interactions are dominant,

$$E_3 = -8t_{+-}^2/U''. \quad (16)$$

Figure 16 shows that for three particles in the three-site system as described in the basis of spherical harmonics, analytic approximations are in agreement with numerical solutions obtained by the author and graduate student co-author. Importantly, at the experimentally relevant $U = U_0$, the virtual hopping approximation of Equation (16) agrees with the numerical solution far better than the independent-particle approximation of Equation (15). This places the system in the strongly-correlated regime. Moreover, this yields insight about the types of models applicable to the system. The independent-particle approximation of Equation (15) is based on Stoner magnetism, which considers single-particle band magnetism and which has been used for similar purposes as this work [5]. However, Figure 16 suggests that the virtual hopping approximation of Equation (16), which is based on the effective Heisenberg model of quasi-localized d -electrons, is a much better approximation for our system.

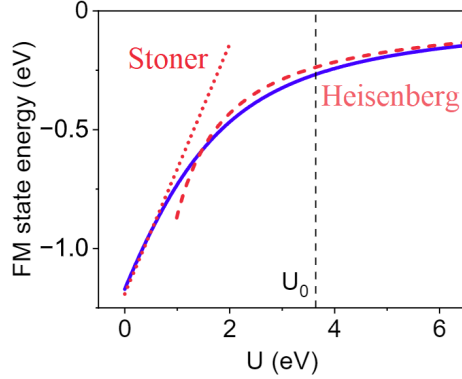


Figure 16: State energy as a function of U for the three site model with two orbitals and one particle per site. Figure is from [11]. The red dots represent the independent-particle Stoner approximation of Equation (15), the red dashes represent the high- U limit approximation of Equation (16), and the solid blue curve represents the numerical solution. Notice that at the experimentally-relevant U_0 , the Heisenberg virtual hopping approximation agrees with the numerical solution.

Remarkably, this three-particle state can be interpreted in terms of two-particle correlations. Quoting the adviser's analytic calculations [11], we can describe the three-particle system with the wave function

$$\psi_{3,s} = \frac{1}{2\sqrt{6}} \sum \sigma c_{n-2,\sigma,s}^\dagger c_{n-1,\sigma,s}^\dagger c_{n,\sigma',s}^\dagger |0\rangle, \quad (17)$$

where the symbols follow the definitions of Equation (12). The (normalized) component of this state with $n = 3$ is

$$\psi'_{3,s} = \frac{1}{2} \left(c_{1,+s}^\dagger c_{2,+s}^\dagger - c_{1,-s}^\dagger c_{2,-s}^\dagger \right) \left(c_{3,+s}^\dagger + c_{3,-s}^\dagger \right) |0\rangle. \quad (18)$$

This state is a product of the state d_{xy} on site 3 and an orbitally ferromagnetically-correlated singlet state [11] on sites 1 and 2,

$$\psi_{12,s} = \frac{1}{\sqrt{2}} \left(c_{1,+s}^\dagger c_{2,+s}^\dagger - c_{1,-s}^\dagger c_{2,-s}^\dagger \right) |0\rangle. \quad (19)$$

In other words, for the three-site model, if two sites are correlated then the third site cannot be correlated. In the language of interference patterns and visualizing via Figure 15, orbitals $d_{x^2-y^2}$ on sites constructively interfere, but the remaining orbital d_{xy} on site 3 cannot also constructively interfere with the other orbitals. The claims of Equation (18) and Equation (19) are consistent with the two-particle correlations of Figure 12. Moreover, starting from the components corresponding to the states $n = 1$ and $n = 2$ would yield the same results, with the indices cycled. Because of this frustration, the three-site model can be reduced to the two-site model. In the spherical harmonic basis, we describe these two-site orbital correlations ferromagnetically.

Putting together the results from the derivation so far, there is frustration between the orbital symmetries and crystal symmetries. The virtual hopping ground state wavefunction of Equation (17) is a superposition of

pairwise ferromagnetically-correlated orbital singlets which are uncorrelated with the third site [17]. Because this frustration prevents complete ferromagnetic orbital ordering, we can describe the ultrathin films of late transition metals through means of an orbital liquid state, with local correlations but a lack of long-range orbital ordering. The conclusion of an orbital liquid state for our systems is a key result of this work.

3.3.3 Application to PMA

To summarize, the key result of this theoretical discussion is the orbital liquid state from the frustration effects described earlier. However, because the orbital moments are quenched in this orbital liquid state, it is difficult to observe this state directly by experiment. In our theoretical paper [11], we provide examples of predictions our model makes in the context of spin-orbit coupling (SOC) and applications to perpendicular magnetic anisotropy (PMA), which is dependent on SOC. More specifically, PMA results from spin coupling to non-classical orbital states that do not have in-plane orbital moment projection [17]. As was shown for thin films of late transition metals in Section 2, large PMA is often observed experimentally, and it is an important property in terms of technological relevance in magnetic memory storage devices.

To clarify the origins of PMA in our systems, consider the energy of spin-orbit-coupling,

$$E_{SOC} = -\lambda \vec{S} \cdot \vec{L}, \quad (20)$$

where λ is positive in Pt, \vec{S} is the spin moment, and \vec{L} is the orbital moment. Consider, as was inferred previously, that d_{+2} and d_{-2} are the dominant orbitals. Then, to minimize the energy of the system, we expect \vec{S} to align with these orbital moments as shown in Figure 17.

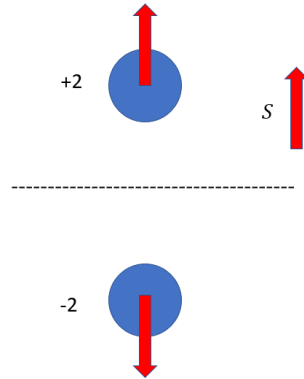


Figure 17: Cartoon schematic of the origin of PMA in our systems. The blue circles represent the d_{+2} and d_{-2} orbitals, with their orbital moments shown as arrows. The S arrow shows the orientation of the spin moment.

Moving on, we analyze the SOC Hamiltonian in the basis of spherical harmonics,

$$\hat{H}_{SOC} = 2\lambda \sum_{\vec{n}, \sigma, s} s \cdot \sigma \hat{n}_{\vec{n}, \sigma, s} \quad (21)$$

using the same language as the previous Hamiltonians, where $\lambda = 40$ meV for Ni [2]. The adviser's analytic calculations applying Equation (21) through first-order perturbation theory obtained that in the limit of negligible SOC,

$$E_t = \frac{U''}{2} - \sqrt{\left(\frac{U''}{2}\right)^2 + 4t_{+-}^2}, \quad (22)$$

and accounting for the contribution to the energy from SOC, $E = E_t + E_{SOC}$ where

$$E_{SOC} = \frac{8\lambda^2}{E_t} \left(1 + \frac{E_t}{U'' - 2E_t}\right). \quad (23)$$

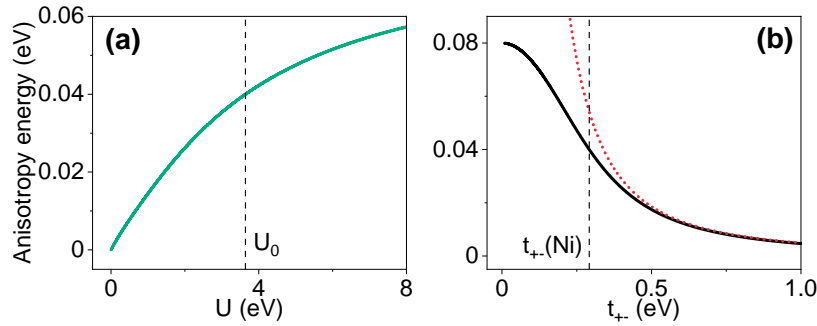


Figure 18: Two-site PMA energy as a function of interaction U and hopping parameter t_{+-} . Figure is from [11]. We use $\lambda = 40$ meV, $J = 0.21U_0$, and in (b), $U'' = 2.87$ eV. Solid curves show numerical solutions; the dotted red curve in (b) is the analytic approximation given by Equation (23).

Consider Figure 18, which compares the adviser's analytic calculations to numerical simulations. The figure allows visualization of two-site PMA energy as a function of interaction and hopping, and we see that the anisotropy energy increases as U increases. And as hopping decreases, PMA increases due to the smaller virtual hopping contribution that flips orbital moments [17]. Experimentally, Figure 18b agrees with these mechanisms and is more tangible, as we can control hopping through the introduction of impurities in the deposition of the films or through lattice strain (for example, by stretching the material). Thus, our theoretical work [11] predicts that PMA in ultrathin films of late transition metals can be controlled by experimentally varying hopping parameters. Moreover, it is a demonstration that correlations can be harnessed to tune properties of technologically relevant materials.

3.3.4 Role of Pt

Further analysis of CoFeB ultrathin films can be made by considering the role that Pt (and its interface with the ferromagnetic CoFeB layer) plays in our systems. Firstly, we should expect orbital correlations across the Pt/CoFeB interface, as orbitally-selective virtual hopping across the interface stabilizes antiferromagnetic orbital correlations [17]. An example of this virtual hopping is shown in Figure 19b.

An interesting feature from the BLS measurements of Section 2 is the low Landé g -factor of $g = 1.78$ at zero current. As was discussed previously, at such a low g -factor, the spin and orbital moments should be parallel. It has been shown [6] (via extrapolation of experimental measurements) that Pt could have a g -factor as low as $g = 1.65$. So it is possible that Pt in the sample used for BLS causes the g -factor to drop so low in the low-current regime.

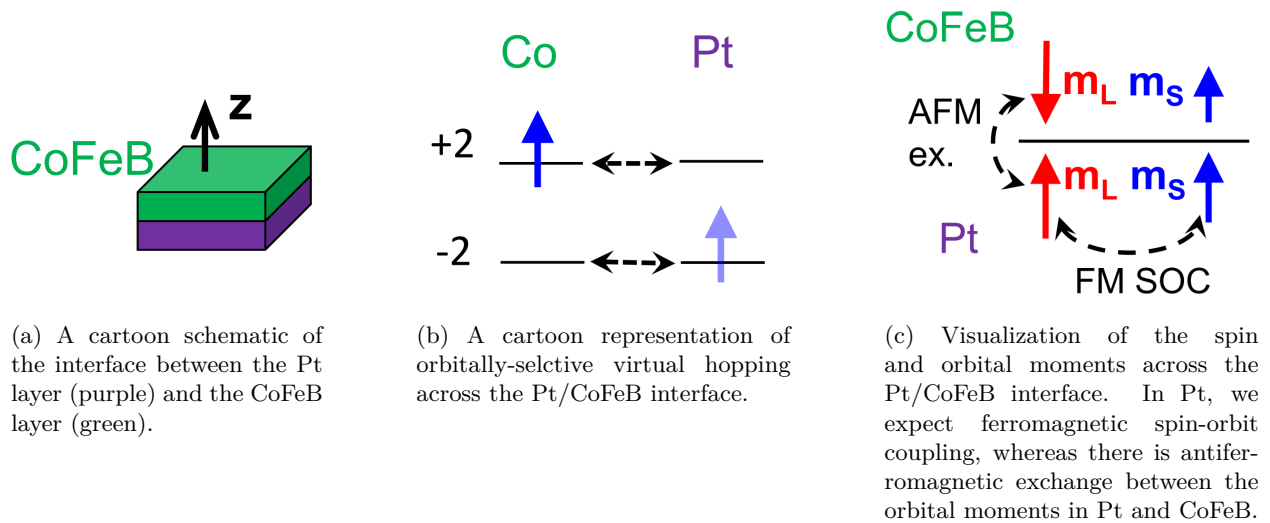


Figure 19: Visual aids of our most recent understanding of the role of Pt. Figures were created by the adviser [17].

It is also possible that Pt contributes largely to the mismatch in "wiggle" signatures between AHE and MOKE measurements. The "wiggle" feature in AHE likely originates from the spin polarization in Pt induced by orbital polarization due to SOC, whereas MOKE is insensitive to the magnetization of Pt [17].

4 Conclusions

To summarize, in Section 2 we show experimental evidence that orbital magnetism is a key component of anomalous features observed in AHE measurements of ultrathin films of Co/Ni and CoFeB and BLS measurements. We compare and contrast these measurements with MOKE measurements of CoFeB.

Our theoretical work determines that orbital correlations are present in ultrathin films of late transition metals, and that in an fcc structure, geometric frustration results prevents ferromagnetic orbital ordering and results in an orbital liquid state. Comparison between Stoner-like analytics, Heisenberg-like analytics, and numerical solutions shows that at relevant interaction parameters, the Stoner model is insufficient and the virtual hopping approximation is much more appropriate. Applications of this orbital liquid state to SOC-dependent phenomena such as PMA are discussed, and the role of Pt in our structures is explored in the context of our experimental observations.

References

- [1] J. Bardeen, L. N. Cooper, and J. R. Schrieffer. Theory of superconductivity. *Phys. Rev.*, 108:1175–1204, Dec 1957.
- [2] J. Büneemann, F. Gebhard, T. Ohm, S. Weiser, and W. Weber. Spin-orbit coupling in ferromagnetic nickel. *Phys. Rev. Lett.*, 101:236404, Dec 2008.
- [3] Luca de' Medici. Hund's coupling and its key role in tuning multiorbital correlations. *Phys. Rev. B*, 83:205112, May 2011.
- [4] Patrick Fazekas. *Lecture Notes on Electron Correlation and Magnetism*. World Scientific, 1999.
- [5] G.W. Fernando, A.N. Kocharian, R.E. Watson, and M. Weinert. Stoner criterion of ferromagnetism and moment saturation in the hubbard model with an applied magnetic field. *Physica B: Condensed Matter*, 230-232:509–512, 1997. Proceedings of the International Conference on Strongly Correlated Electron Systems.
- [6] G. Fischer and M.J. Besnus. g factor and magnetization measurements of nickel-platinum alloys. *Solid State Communications*, 7(21):1527–1530, 1969.
- [7] David J. Griffiths. *Introduction to Quantum Mechanics (2nd Edition)*. Pearson Prentice Hall, 2nd edition, April 2004.
- [8] David J. Griffiths. *Introduction to Electrodynamics*. Pearson, 2013.
- [9] Walter A. Harrison. *Electronic Structure and the Properties of Solids: The Physics of the Chemical Bond*. Dover Publications, New York, 1989.
- [10] Sergei Ivanov, Vladislav E. Demidov, Sergej O. Demikritov, and Sergei Urazhdin. Orbital magnetism in ultrathin films of cofeb and its control by spin current. APS Virtual March Meeting, 2023.
- [11] Sergei Ivanov, Joshua Peacock, and Sergei Urazhdin. Orbital correlations in ultrathin films of late transition metals. *Physical Review Materials*, 7(1):014404, 2023.
- [12] Nikolai B. Kopnin. Introduction to the theory of superconductivity cryocourse 2009. Helsinki, Finland, 2009.
- [13] Kliment I Kugel' and D I Khomskii. The jahn-teller effect and magnetism: transition metal compounds. *Soviet Physics Uspekhi*, 25(4):231, apr 1982.

-
- [14] Sam Mugiraneza and Alannah M. Hallas. Tutorial: A beginner’s guide to interpreting magnetic susceptibility data with the curie-weiss law. *Nature Communications Physics*, 2022.
- [15] Eva Pavarini. *The physics of correlated insulators, metals, and superconductors lecture notes of the Autumn School on Correlated Electrons 2017*. Forschungszentrum Julich GmbH, Julich, 2017.
- [16] Joshua Peacock, Sergei Ivanov, and Sergei Urazhdin. Orbital correlations in ultrathin films of late transition metals. PhysCon Conference, Washington, DC, USA, 2022.
- [17] Joshua Peacock, Sergei Ivanov, and Sergei Urazhdin. Orbital liquid state in ultrathin Pt/CoFeB films. APS March Meeting, Las Vegas, Nevada, USA, 2023.
- [18] Joshua Peacock, Alexander Mitrofanov, Guanxiong Chen, Sergei Ivanov, and Sergei Urazhdin. Non-classical orbital magnetism in ultrathin transition metal films. APS March Meeting, Chicago, Illinois, USA, 2022.
- [19] A Sherman. Hubbard-kanamori model: spectral functions, negative electron compressibility, and susceptibilities. *Physica Scripta*, 95(9):095804, aug 2020.
- [20] J. C. Slater and G. F. Koster. Simplified lcao method for the periodic potential problem. *Phys. Rev.*, 94:1498–1524, Jun 1954.